electronics

MDPI

Article

Frequency Stability Analysis and Charging Area Expanding Optimal Design for Matrix Coupling Mechanism in Wireless Power Transfer System

Jincheng Jiang and Zhenya Meng *

College of Automation, Chongqing University of Posts and Telecommunications, Chongqing 400065, China; jiangjinc@cqupt.edu.cn
* Correspondence: mengzy@cqupt.edu.cn

Abstract: The matrix coupling mechanism brings flexibility and reliability to energy supply in the form of multiple transmitting coils and is now favored in most wireless energy transmission applications, such as wireless charging boards for mobile phones, inspection robots, and so on. However, the process of considering the layout of the matrix coupling mechanism and the output performance based on the target in space is very complex, while also taking into account the need to avoid impedance changes caused by cross-interference between each unit, which can lead to frequency inconsistency. This paper proposes a design method based on space charging area expansion for matrix coupling mechanisms, and on this basis, it focuses on analyzing the impedance mismatch phenomenon caused by cross mutual inductance and inconsistent mutual inductance between coil units, in order to obtain the optimal topology to avoid frequency drift as much as possible. Finally, the effectiveness of the method is validated through simulation and experiments.

Keywords: wireless power transfer; matrix coupling; charging area expanding; frequency stability

check for updates

Citation: Jiang, J.; Meng, Z. Frequency Stability Analysis and Charging Area Expanding Optimal Design for Matrix Coupling Mechanism in Wireless Power Transfer System. *Electronics* **2024**, *13*, 1312. https://doi.org/10.3390/electronics13071312

Academic Editor: Ahmed Abu-Siada

Received: 5 January 2024
Revised: 29 March 2024
Accepted: 29 March 2024
Published: 31 March 2024

Copyright: © 2024 by the authors. Licensee MDPI, Basel, Switzerland. This article is an open access article distributed under the terms and conditions of the Creative Commons Attribution (CC BY) license (https://creativecommons.org/licenses/by/4.0/).

1. Introduction

Wireless power transfer (WPT) technology based on magnetic field coupling has been widely used in fields such as electric vehicles, household appliances, underwater equipment, medical implants, and consumer electronics due to its relatively mature mechanism understanding, comprehensive practical technology system, simple and easy system topology, stable energy transfer process, and good robustness [1,2]. At present, there are a large number of wireless charging products for consumer electronic devices such as smartphones, tablets, Bluetooth earphones, smartwatches, etc. on the market, which greatly facilitates user experience [3,4].

However, there are difficulties in the application and promotion of wireless power supply technology, and the core reason is that traditional wireless charging forms have not brought users a breakthrough experience. Traditional magnetic coupling wireless power transfer technology usually only has one primary coil and one secondary coil. Basic figures to illustrate the difference between one and multiple coils are shown in Figure 1. Actually, for some high-power application scenarios, the power level of the one-to-one mode is limited and needs to withstand greater voltage and current stress, and there is not enough flexibility in some application places [5,6]. The limitations of the one-to-one WPT system in the charging area have led people to adopt the coil array method to expand the charging range, and the method of connecting multiple transmitting coils in parallel with a single input source or one primary coil with one excitation source has been utilized. The matrix coupling mechanism or multi-excitation unit wireless power transfer system (MEU-WPT) is favored by many applications, such as distributed-track wireless charging cars, inspection robots, drones, wireless charging platforms for mobile phones, and so on, due to its high power capacity, flexibility, and low current and voltage stress [7–9].

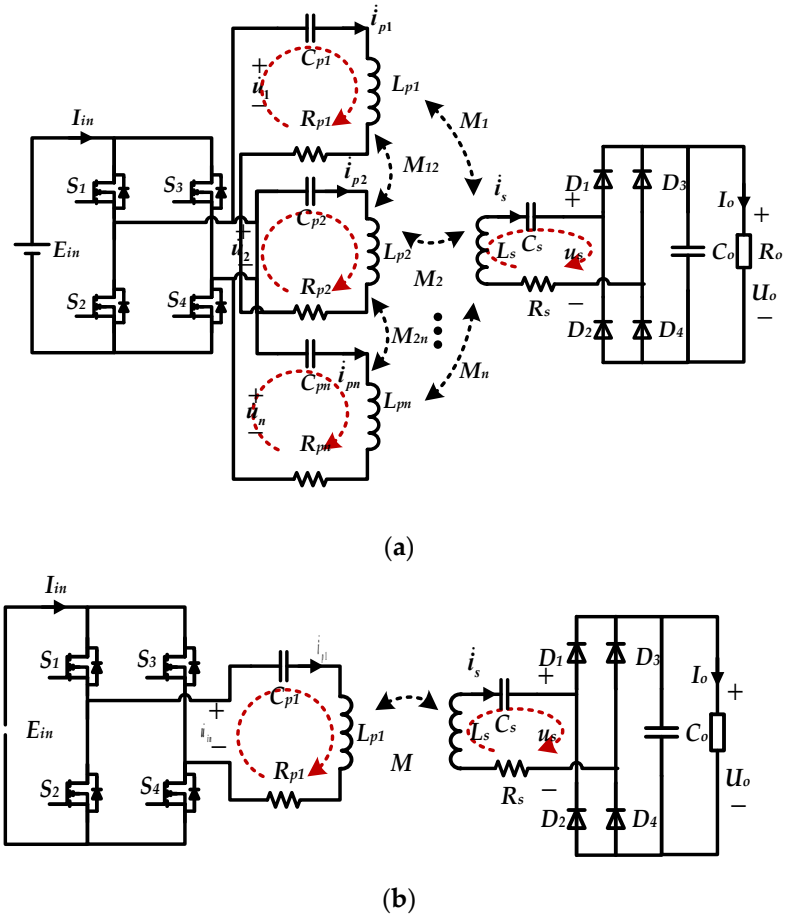

Figure 1. Structure of traditional WPT and proposed system. (**a**) Proposed system with matrix coil. (**b**) Traditional system.

To date, research based on multiple transmitting or receiving coils mainly focuses on the following aspects: (1) modeling and solving of complex nonlinear systems [10–12]. The most commonly used modeling and analysis methods currently include coupled-mode theory [10], mutual inductance coupling theory [11], and two-port theory [12]; (2) coupling mechanisms and parameter design [13,14]. Based on the mapping relationship of model functions, to configure the modal parameters of the system, combined with various corresponding constraint conditions, designing the actual modal parameters of the WPT system is a crucial step; (3) power distribution and control [15,16]. In the wireless charging process of various application scenarios, the change of the coupling coefficient during dynamic charging and the interference of environmental factors must be considered. Although the above research has to some extent improved the performance of MEU-WPT systems through parameter optimization and control circuits, there has been no reasonable planning and utilization of the layout of coil units. Most coupling mechanisms are based on the most common pattern printing or an equal amount of winding. However, in the above research, there was no clear determination of the charging area boundary for the MEU-WPT system. Further in-depth research is needed on how to define an effective charging area, how to design a reasonable layout and expand the area based on the characteristics of the coil matrix, and how to avoid interference between matrix elements during the working phase.

To achieve the best system performance, many design objectives must be included. The power level, efficiency, and misalignment tolerance should be considered in total. In addition, because all shape parameters of these multiple excitation coils must be considered, the design work will become more complex. Among the previous works on coupling mechanism design for MEU-WPT systems, paper [17] proposed a novel multi-coil WPT

system to enhance power transfer efficiency. It can overcome the misalignment problem and maintain high power transfer efficiency. In paper [18], based on the lumped element circuit model, the efficiency, current gain, and voltage gain calculations of multi-coil magnetic resonance wireless power transfer systems are given. And paper [19] proposed a scalable printed circuit board (PCB)-based coil design for electric vehicle (EV) wireless power transfer. Paper [20] proposed a multi-layer coil (MLC) for wireless charging for small electronic devices (SED), such as implantable medical devices (IMD) and wearable devices. And paper [21] presents a design method for a multi-transmitter wireless power transfer (WPT) system that aims to achieve stable and high power transfer efficiency (PTE) across a wide range. However, previous studies did not provide a specific definition of the actual charging area, and the question of how to maximize the charging area of the matrix coil is an urgent problem that needs to be solved. At the same time, the optimization design and adaptability of matrix coils under different layouts still need to be reconsidered. Moreover, further in-depth research is needed to design a reasonable layout and expand the area based on the characteristics of the coil matrix with interference considered between matrix elements during the working state, such as the impact on the frequency characteristics and output characteristics of the system.

This paper proposes an optimization design method for expanding the charging area of matrix coils and evaluates the frequency characteristics and interference between each coil unit while considering multi-objective parameters. It provides a reasonable approach for the topology selection of matrix coil coupling mechanisms with frequency drifting analysis. The second section constructs the system model, the third section calculates and derives the mutual inductance of the matrix coil layout, and the fourth section analyzes the interference characteristics of the coil unit data and provides a comprehensive design idea based on the previous calculation formulas. Finally, the method is validated and explained.

2. Modeling of Proposed System

According to the system structure shown in Figure 1a, S_1–S_4 are the switching transistors of the inverter circuit. On the primary side, C_{pi} is the compensated capacitor, $L_{p\mathrm{i}}$ is the inductance of the primary coil, and $R_{p\mathrm{i}}$ is the internal resistance of coils. On the secondary side, similarly, C_s is the compensated capacitor, L_s is the inductance of the pick-up coil, and R_s is its internal resistance. D_1–D_4 are the diodes of the rectifier. And C_o is the filter capacitor of the load R_o. E_{in} is the input voltage, $\dot{u}_i$ is output voltage of the inverter, and I_{in} is the input current of the inverter. $\dot{i}_{pi}$ is the resonant current of each primary coil. i_s is the pick-up current. u_s is the input voltage of the rectifier, and I_o, U_o are the current or voltage of the load. In order to balance magnetic field distribution, each primary coil has the same parameter in the multi-excitation coil matrix. The system parameters are set as $C_{p1} = C_{p2} = \ldots = C_{pn}$, $L_{p1} = L_{p2} = \ldots = L_{pn}$, $R_{p1} = R_{p2} = \ldots = R_{pn}$. Take the series-series-type topology as an example, and the primary side and pick-up side operate at an identical angular frequency ω, which can be defined by

$$\omega = \frac{1}{\sqrt{L_s C_s}} = \frac{1}{\sqrt{L_{pn} C_{pn}}} \tag{1}$$

According to KVL's law, the relationship between the currents and voltages can be derived as

$$\begin{cases} \dot{u}_1 = j\omega(L_{p1}+\mathrm{C}_{p1} + R_{p1})\dot{i}_{p1} + j\omega M_{12}\dot{i}_{p2} + j\omega M_{1i}\dot{i}_{pi} + \ldots + j\omega M_1\dot{i}_s \\ \dot{u}_2 = j\omega(L_{p2}+\mathrm{C}_{p2} + R_{p2}) + j\omega M_{12}\dot{i}_{p1} + j\omega M_{2i}\dot{i}_{pi} + \ldots + j\omega M_2\dot{i}_s \\ \vdots \\ \dot{u}_\mathrm{n} = j\omega(L_{pn}+\mathrm{C}_{pn} + R_{pn}) + j\omega M_{1n}\dot{i}_{p1} + j\omega M_{ni}\dot{i}_{pi} + \ldots + j\omega M_n\dot{i}_s \\ 0 = j\omega M_1\dot{i}_{p1} + j\omega M_2\dot{i}_{p2} + \ldots + j\omega M_n\dot{i}_{pn} + \left(\frac{8}{\pi^2}\mathrm{R_o}+\mathrm{R}_s + L_s+\mathrm{C}_s\right)\dot{i}_s \end{cases} \tag{2}$$

Using Formula (1) as the principle of resonant matching and ignoring cross-coupling, the circuit equation of the system can be simplified in an ideal situation.

$$\begin{bmatrix} \dot{u}_1 \\ \dot{u}_2 \\ \vdots \\ \dot{u}_n \\ 0 \end{bmatrix} = \begin{bmatrix} R_{p1} & 0 & \cdots & 0 & j\omega M_1 \\ 0 & R_{p2} & \cdots & 0 & j\omega M_2 \\ \vdots & \vdots & \vdots & \vdots & \vdots \\ 0 & 0 & \cdots & R_{pn} & j\omega M_n \\ j\omega M_1 & j\omega M_2 & \cdots & j\omega M_n & R_o + R_s \end{bmatrix} \begin{bmatrix} \dot{i}_{p1} \\ \dot{i}_{p2} \\ \vdots \\ \dot{i}_{pn} \\ \dot{i}_s \end{bmatrix} \tag{3}$$

Therefore, the equivalent impedance of the primary side could be expressed as

$$\begin{cases} Z_{p1} = \dfrac{u_{p1}R_p^2(R_o+R_s)+u_{p1}\omega^2 R_p \sum_{i=1}^{n} M_i^2}{R_p(R_o+R_s)u_1+\omega^2(u_1\sum_{i=1}^{n} M_i^2-M_1\sum_{i=1}^{n} M_i u_i)} \\ Z_{p2} = \dfrac{u_{p2}R_p^2(R_o+R_s)+u_{p2}\omega^2 R_p \sum_{i=1}^{n} M_i^2}{R_p(R_o+R_s)u_2+\omega^2(u_2\sum_{i=1}^{n} M_i^2-M_2\sum_{i=1}^{n} M_i u_i)} \\ \vdots \\ Z_{pn} = \dfrac{u_{p3}R_p^2(R_o+R_s)+u_{p3}\omega^2 R_p \sum_{i=1}^{n} M_i^2}{R_p(R_o+R_s)u_n+\omega^2(u_n\sum_{i=1}^{n} M_i^2-M_n\sum_{i=1}^{n} M_i u_i)} \end{cases} \tag{4}$$

And the output power of multi-excitation coils could be obtained by

$$P_{out} = \left(\frac{\omega \sum_{i=1}^{n} M_i u_i}{R_p(R_o+R_s)+\omega^2 \sum_{i=1}^{n} M_i^2}\right)^2 R_o \tag{5}$$

3. Matrix Coil Optimal Design Method

Before the design, the final target is determined to improve the output characteristics; efficiency is especially considered first. To design the coupling mechanism based on a multi-excitation coil matrix, the size of the receiver coil and transmission distance should be determined. At the same time, the size of every single excitation and the number of coils will determine the output characteristics of the system. Figure 2 shows a wireless power transfer system with three primary coils and four primary coils.

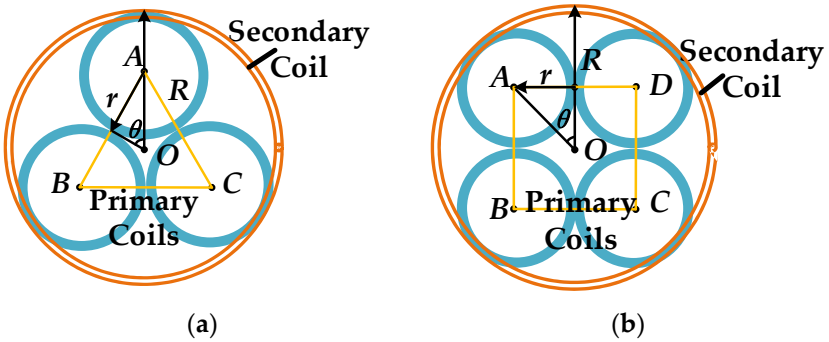

Figure 2. Different layouts of multi-excitation coil matrix: (**a**) with 3 primary coils; (**b**) with 4 primary coils.

With a different layout, only the projection area of the secondary coil containing the largest number of excitation coils is considered as the effective position to analyze. In Figure 2, R is the radius of the secondary coil, and r is the radius of every single primary coil. To reduce the complexity of parameter design, overlapping primary coils are not

considered. Because of the arrangement in the same plane, the cross-coupling is small enough to ignore.

Spatial modeling of the coupling mechanism is built for the multi-excitation coil matrix in Figure 2. Take Figure 2a as an example. The multi-excitation coils are built by a regular triangle ΔABC if the centers of excitation coils are connected. Similarly, there is a square $ABCD$ in Figure 2b. Drawing the circles at vertices of the regular polygon with n edges, all the circles are regarded as the primary coils. At the same time, all the outmost primary coils are within the region of the pick-up coil. The relationship between the radius r of the primary coil and the radius of the secondary coil R could be derived as

$$\begin{array}{l} R = r/n \ (n = 1, 2) \\ R = r(1 + \frac{1}{\sin(\pi/n)})(n = 3, 4 \ldots) \end{array} \tag{6}$$

To calculate M, the tracks of the planar in ductors are assumed as constant current-carrying filaments, as shown in Figure 3.

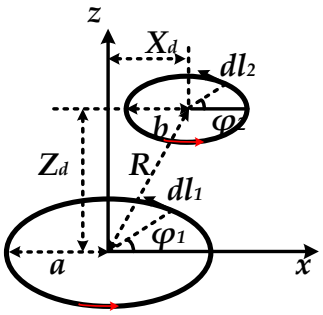

Figure 3. Coordinate establishment of carrying filament.

During the charging process, the output characteristics of the system are evaluated by analyzing the changes in the coupling coefficient. From the sources in [22,23], Neumann's equation is employed to calculate mutual inductance:

$$M_{ij} = \frac{\mu_0}{4\pi} \oint_{c1} \oint_{c2} \frac{1}{R} d\vec{l}_1 \cdot d\vec{l}_2 \tag{7}$$

where

$$R = \sqrt{a^2 + b^2 + Z_d^2 + X_d^2 - 2ab\cos(\varphi_1 - \varphi_2) + 2X_d b\cos\varphi_2 - 2X_d a\cos\varphi_1} \tag{8}$$

In the above equation, μ_0 is the vacuum magnetic permeability, M_{ij} is the mutual inductance between single-turn current-carrying wires c_1 and c_2, R is the center distance, a and b are the radii of the two current-carrying wires, Z_d is the vertical distance, and X_d is the lateral center offset distance. φ_1, φ_2 is the horizontal offset angle, introduced by these three equations:

$$\begin{array}{c} \xi = \frac{2ab}{a^2+b^2+Z_d^2} \\ \lambda = \frac{2xa}{a^2+b^2+Z_d^2+X_d^2} \\ \phi = \frac{2xb}{a^2+b^2+Z_d^2+X_d^2} \end{array} \tag{9}$$

Equation (9) can be expressed as

$$\begin{array}{c} M_{ij} = \frac{\mu_0 ab}{4\pi\sqrt{a^2+b^2+X_d^2+Z_d^2}} \int_{\varphi_2=0}^{\varphi_2=2\pi} \int_{\varphi_1=0}^{\varphi_1=2\pi} \cos(\varphi_1 - \varphi_2) \times [1 - (\gamma\cos(\varphi_1 - \varphi_2) \\ +\lambda\cos\varphi_1 - \phi\cos\varphi_2)]^{-1/2} d\varphi_1 d\varphi_2 \end{array} \tag{10}$$

where $\gamma = X_d^2/(a^2 + b^2 + Z_d^2 + X_d^2)$. According to the paper in [24], the self-inductance of a single primary coil could be derived as

$$\begin{array}{c} d_{avg} = 0.5(D_{\max} + D_{\min}) \\ \beta = \frac{D_{\max} - D_{\min}}{D_{\max} + D_{\min}} \\ L = \frac{\mu_0 N^2 d_{avg} m_1}{2}(\ln\frac{m_2}{\beta} + m_3\beta + m_4\beta^2) \end{array} \tag{11}$$

where D_{max} is the maximum diameter of the coil, and D_{min} is the minimum diameter of the coil. μ_0 is the permeability of free space, and m_1~m_4 are fitting parameters, which are determined by the shape of a coil. Paper [24] notes that for a circular coil, m_1 = 1.0, m_2 = 2.46, m_3 = 0, and m_4 = 0.2. Moreover, according to paper [25], the DC resistance of a solid-round wire winding and the skin depth of the conducting wire δ_w are described by

$$\begin{array}{c} R_{dc} = \frac{4\rho_w N l_T}{\pi d^2} \\ \delta_w = \sqrt{\frac{\rho_w}{\pi\mu_0 f}} \end{array} \tag{12}$$

where ρ_w is the winding conductor resistivity, N is the total number of turns in the inductor, and l_T is the mean turn length. d is the diameter of a bare solid-round wire. From paper [25], the AC-to-DC winding resistance ratio F_R as a function for a solid-round wire winding with η = 0.9 and several numbers of layers N_l could be described by

$$\begin{array}{c} F_R = 1 + \frac{\eta^2(5N_l^2 - 1)}{45}(\frac{\pi}{4})^3(\frac{d}{\delta_w})^4 \\ R_{ac} = R_{dc}F_R \end{array} \tag{13}$$

Consider the receiving power from multi-excitation coils as an approximate linear superposition. When the phase of the resonant current on the primary coil is the same, the magnitude of a magnetic field can be expressed by the sum of the coupling coefficient of every single excitation coil. For traditional one-to-one WPT systems, the expression for the induced voltage of the pickup coil is $j\omega M\dot{i}_p$. Therefore, for a WPT system with multiple transmitting coils, the voltage of the secondary side pickup coil is a linear superposition of the voltage sensed from each transmitting coil. When n excitation units are working simultaneously, the value of the picked-up voltage on the secondary side can be expressed as $\sum_{i=1}^{n} j\omega M_i\dot{i}_{pi}$. Moreover, the definition of the coupling coefficient for the WPT system is known to be $k = M/(\sqrt{L_p * L_s})$. It is also known that the coupling coefficient for WPT systems is defined as

$$|\dot{u}_s| = \left|\sum_{i=1}^{n} \omega M_i\dot{i}_{pn}\right| = \left|n\omega k_n\sqrt{L_{pn}L_s}\sum_{i=1}^{n}\dot{i}_{pn}\right| \tag{14}$$

For a WPT system with a coil matrix, according to Figure 1, the loss of its coupling mechanism can be expressed as

$$\begin{array}{c} P_{loss} = \sum_{i=1}^{n}\left|\dot{i}_{pi}\right|^2 R_{pi} + \frac{\left|\sum_{i=1}^{n} j\omega M_i\dot{i}_{pi}\right|^2}{(R_o + R_s)^2}R_s \\ P_{out} = \frac{\left|\sum_{i=1}^{n} j\omega M_i\dot{i}_{pi}\right|^2}{(R_o + R_s)^2}R_o \end{array} \tag{15}$$

According to (12) and (13),

$$\begin{array}{l} R_{pi} = R_{dc\_i} + R_{ac\_i} \\ R_s = R_{dc\_s} + R_{ac\_s} \\ R_o = \frac{8}{\pi^2}R_L \end{array} \tag{16}$$

The formula above only considered the outmost coils that are on the vertex of the regular polygon. In this case, due to the central symmetry, the coupling coefficients k_n are the same. When all the input currents are the same, $n{*}k_n$ is used to evaluate the power transmission capability. Once the coils of the outmost layer have enough coupling ability, the whole multi-excitation coil matrix is proven to be effectively used. Furthermore, the loss on the multi-excitation coils must be analyzed at the same time. When the coil parameters are consistent with the coupling coefficient of each coil, the internal resistance of the coil is equal, and $\sum_{i=1}^{n} k_i = n * k_n$. The losses P_{loss} on the coupling mechanism are calculated under the condition of the same power output to evaluate the power-saving capability. Set P_{target} as the target value of the power. When $P_{out} = P_{target}$, the above equation can be written as

$$\begin{gathered} P_{loss} = \frac{8P_{target}R_s}{\pi^2 R_L} + \frac{8P_{target}R_p\left(R_s + \frac{\pi^2}{8}R_L\right)^2}{n\omega M_n \pi^2 R_L} \\ \eta = \frac{P_{out}}{P_{loss}+P_{out}} \end{gathered} \tag{17}$$

To design the multi-excitation coil matrix, only the following equations need to be satisfied, that is, the minimum coupling coefficients of the secondary coil and transmitting coil that is farthest from the center of the charging area need to be greater than the target value at first. Secondly, the efficiency of the whole coupling mechanism should be greater than the target value.

$$\begin{gathered} k_n \geq k_{target} \\ P_x \geq P_{target} \\ P_{x0} = P_{target} \\ \eta \geq \eta_{target} \end{gathered} \tag{18}$$

According to the data analysis in the previous section, the maximum charging area is defined as the maximum shadow area projected on the plane XOY by the output power surface greater than or equal to the rated power when all excitation units output the same maximum current. Based on the parameter design in the previous text, the known conditions are determined as the size of the primary coil a, the size of the secondary coil b, the transmission distance z, etc. The coordinates of the primary coil are defined as $(x_i, y_i, 0)$, the spatial coordinates of the secondary coil as (x_s, y_s, z_s), and the constraints on the coordinates of the primary coil as

$$\forall\sqrt{(y_j - y_i)^2 + (x_j - x_i)^2} \geq a, (i \neq j) \tag{19}$$

According to the mutual inductance Equation (10) and Figure 3, it can be inferred that the mutual inductance function is related to the variable X_d (the plane distance between the center of the primary and secondary coils, $X_d = \sqrt{(x_s - x_i)^2 + (y_s - y_i)^2}$). Under a given transmission height condition Z_d, define function $M((x_s - x_i),(y_s - y_i))$ as the mutual inductance equation at a certain height. And the power distribution surface function $P(x_s, y_s)$ at any position can be obtained by using the picked-up voltage Equation (14):

$$P_{(x_s,y_s)} = \frac{\left[\left|\omega \dot{i}_{p\_\max} \sum_{i=1}^{n} M_{is}((x_s - x_i),(y_s - y_i))\right|\right]^2 R_o}{(R_o + R_s)^2}, (i = 1, 2, \ldots, n) \tag{20}$$

For matrix coils, when the coil currents i_p are in phase, the secondary coil picks up the maximum energy. According to the load power demand, assuming that all coil unit

currents are in phase, at the specified transmission height Z_d, the projection of the surface Equation (20) in space on the XOY plane $z = P_{target}$ can be expressed as

$$\begin{cases} f(x_s, y_s) = \dfrac{\left[\omega i_{p\_\max} \sum_{i=1}^{n} M_{is}((x_s - x_i), (y_s - y_i))\right]^2 R_o}{(R_o + R_s)^2} \\ z = P_{\text{target}} \end{cases} \tag{21}$$

It can be seen that Formula (20) is the power surface function at a given transmission height, whose variables are x_s and y_s in the spatial plane. In Formula (21), the difference between the actual output power at a determined position in space and the target power is defined. When the judgment condition $f(x_s, x_y)$ is greater than or equal to 0, the effective charging area of the power surface can be determined. Furthermore, the Cartesian coordinate system could be converted to a polar coordinate system, and the projection area of the surface (20) on the XOY plane $z = P_{target}$ can be calculated.

The Cartesian coordinate system is converted to a polar coordinate system, and the projected area S of the power distribution surface on the XOY plane can be expressed as

$$S(r, \theta) = \int_0^{2\pi} \int_0^{\varphi(\theta)} f(r\cos\theta, r\sin\theta) r dr d\theta \tag{22}$$

Among $\varphi(\theta)$, in Equation (22), r is the expression of the dependent variable. And the maximum area of this charging area is only related to the distribution of coordinates (x_i, y_i) of each excitation unit when the coupling mechanism parameters and transmission distance are determined.

Therefore, the mathematical expression for expanding the effective charging area can be transformed into

$$\begin{array}{ll} \max & S(r, \theta) \\ \text{s.t.} & \begin{array}{l} k_n \geq k_{\text{target}} \\ P_x \geq P_{\text{target}} \\ P_{x0} = P_{\text{target}} \\ \eta \geq \eta_{\text{target}} \end{array} \end{array} \tag{23}$$

Based on the previous analysis, the coil parameters of multiple excitation units are calculated in sequence according to the given coupling mechanism's constraint relationship and system output indicators, and the optimal design method is determined based on the judgment conditions. This section proposes a flowchart for optimizing the design of incentive units, as shown in Figure 4.

The optimization idea of the flowchart is as follows:

① Determine the size and transmission distance of the primary and secondary coils based on the application background and device appearance, and set the system output characteristic indicators, including the minimum coupling coefficient k_n, rated power P_{target}, and efficiency η target;

② Determine the coupling coefficient of the system in a centrally symmetrical layout using the spatial mutual inductance distribution establishment method (9) analyzed earlier and the coordinate derivation method of the original excitation unit (10). Simultaneously, perform the first step of optimization judgment. If the coupling coefficient of each excitation unit is greater than or equal to k_n, proceed to the next step; otherwise, the number of excitation units will decrease;

③ Based on the coupling mechanism of the current size, refer to Formulas (17) and (20) to further derive the output characteristics of the multiple excitation units. If the output power reaches the rated power target, proceed to the next step;

④ During the loop process, efficiency or comparison is performed on the front and back elements of the data array, and the number of excitation units with higher efficiency is selected;

⑤ By determining the condition $P_{(xs,ys)} = P_{target}$, increase the spacing d_r between the excitation units, calculate the effective charging area, and compare the size of the charging area. If the requirements are not met, re-plan the coil size and repeat the steps to expand the charging range. Finally, use the above method to obtain the final optimized design parameters.

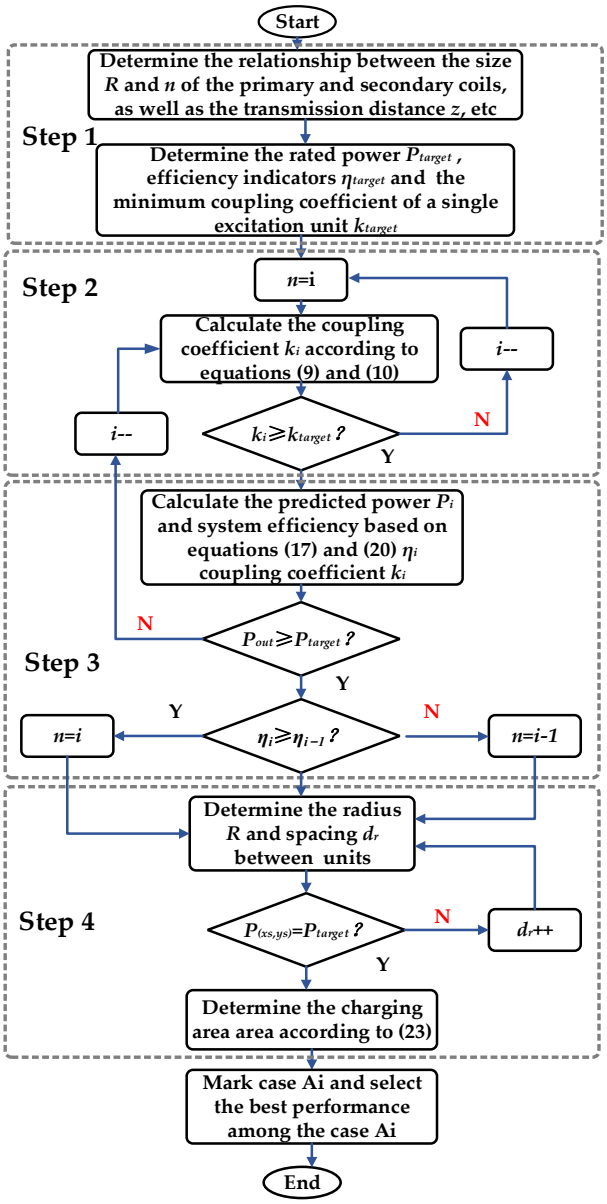

Figure 4. Flow chart of the design method.

4. Frequency Stability Analysis for Matrix Coils

In section III, the analysis is mainly focused on the output characteristics. In order to more intuitively reflect the relationship between the excitation coil and the load, the system equation has been simplified according to the ideal resonant matching situation. As analyzed earlier, the matrix coupling mechanism system is a high-order coupled system, and during the charging process, changes in mutual inductance, load, and even input source can affect the zero-phase operating frequency of each excitation unit (Equation (2)). However, it is not possible to improve the output characteristics of the system by satisfying the zero-phase operating frequency of each excitation unit, because for a pickup end device with a unique resonant frequency, the energy superposition of multiple frequency bands will increase the circuit loss. Taking two adjacent array units as an example, this section

mainly discusses the dynamic characteristic of the system based on the topology types of different input sources and analyzes the design principles of matrix coils with frequency stability as the goal. The design parameters of the system in this section are shown in Table 1.

Table 1. Parameters of the system for stability.

Parameters	Values	Parameters	Values
$L_{p1}L_{p2}$	110 μH	L_s	210 μH
R_{p1}/R_{p2}	0.1 Ω	R_s	0.2 Ω
C_{p1}/C_{p2}	0.52 μF	C_s	0.3 μF
L_{dc} (in parallel-series topology case)	1 mH	R_L	30 Ω
M_{12}	1 μH		

Taking the topology types of voltage (series-series type) and current sources (PS type) as examples, considering the symmetry of matrix coils, the frequency drift phenomenon between the two coils is analyzed with emphasis.

According to Equation (2), the expression for the input impedance of a voltage-type system with series-series topology is as follows, where u_1 and u_2 are the effective values of the primary voltage, respectively:

$$\begin{bmatrix} \dot{i}_{p1} \\ \dot{i}_{p2} \end{bmatrix} = (a_{vs} + b_{vs}\mathrm{j})^{-1} \begin{bmatrix} f_{1\_vs}(u_1, u_2) + g_{1\_vs}(u_1, u_2)\mathrm{j} \\ f_{2\_vs}(u_1, u_2) + g_{2\_vs}(u_1, u_2)\mathrm{j} \end{bmatrix} \tag{24}$$

where

$$\begin{aligned} a_{vs} &= \omega^2 C_p^2[-\omega^2 Z_s L_p^2 + \omega^2 Z_s M_{12}^2 + \omega^2 R_p(M_1^2 + M_2^2) \\ &\quad + Z_s R_p^2] + 2\omega^2 L_p C_p - Z_s \\ b_{vs} &= \omega^2 C_p^2[\omega^3 L_p(M_1^2 + M_2^2) - 2\omega^3 M_1 M_{12} M_2 + 2\omega Z_s L_p R_p] \\ &\quad - \omega C_p[\omega^2(M_1^2 + M_2^2) + 2Z_s R_p] \\ f_{1\_vs}(u_1, u_2) &= \omega^2 C_p^2(-\omega^2 M_1 M_2 u_2 + \omega^2 M_2^2 u_1 + Z_s R_p u_1) \\ g_{1\_vs}(u_1, u_2) &= \omega Z_s C_p(\omega^2 C_p L_p u_1 + \omega^2 C_p M_{12} u_2 - u_1) \\ f_{2\_vs}(u_1, u_2) &= \omega^2 C_p^2(-\omega^2 M_1 M_2 u_1 + \omega^2 M_1^2 u_2 + Z_s R_p u_2) \\ g_{2\_vs}(u_1, u_2) &= \omega Z_s C_p(\omega^2 C_p L_p u_2 + \omega^2 C_p M_{12} u_1 - u_2) \end{aligned} \tag{25}$$

Therefore,

$$\begin{bmatrix} Z_{p1} \\ Z_{p2} \end{bmatrix} = (a_{vs} + b_{vs}\mathrm{j}) \begin{bmatrix} u_1 & 0 \\ 0 & u_2 \end{bmatrix} \begin{bmatrix} [f_{1\_vs}(u_1, u_2) + g_{1\_vs}(u_1, u_2)\mathrm{j}]^{-1} \\ [f_{2\_vs}(u_1, u_2) + g_{2\_vs}(u_1, u_2)\mathrm{j}]^{-1} \end{bmatrix} \tag{26}$$

Similarly, a current-type system with parallel-series (PS) topology can be expressed as

$$\begin{bmatrix} \dot{i}_{p1} \\ \dot{i}_{p2} \end{bmatrix} = (a_{cs} + b_{cs}\mathrm{j})^{-1} \begin{bmatrix} f_{1\_cs}(u_1, u_2) + g_{1\_cs}(u_1, u_2)\mathrm{j} \\ f_{2\_cs}(u_1, u_2) + g_{2\_cs}(u_1, u_2)\mathrm{j} \end{bmatrix} \tag{27}$$

where

$$\begin{aligned} a_{cs} &= \omega^2[R_p(M_1^2 + M_2^2) + Z_s(M_{12}^2 - L_p^2)] + Z_s R_p^2 \\ b_{cs} &= \omega^3(L_p M_1^2 + L_p M_2^2 - 2M_1 M_{12} M_2) + 2\omega Z_s L_p R_p \\ f_{1\_cs}(u_1, u_2) &= \omega^2(M_2^2 u_1 - M_1 M_2 u_2) + Z_s R_p u_1 \\ g_{1\_cs}(u_1, u_2) &= \omega Z_s(L_p u_1 - M_{12} u_2) \\ f_{2\_cs}(u_1, u_2) &= \omega^2(M_1^2 u_2 - M_1 M_2 u_1) + Z_s R_p u_2 \\ g_{2\_cs}(u_1, u_2) &= \omega Z_s(L_p u_2 - M_{12} u_1) \end{aligned} \tag{28}$$

As shown in Figure 5, the frequency drift phenomenon is observed from the perspective of each excitation unit. For different input source types of MEU-WPT systems with different input voltages and coupling coefficients, the frequency characteristic curves of each excitation unit are as follows. Among them, Figure 5a–c shows the current source-type MEU-WPT system, and Figure 5d–f shows the voltage source-type MEU-WPT system. The horizontal frequency range is 20 kHz~200 kHz, and the vertical axis represents the impedance angle of the resonant network of each excitation unit. The system harmonic frequency is 80 kHz.

From Figure 5a–c, it can be seen that the coil current phase of the current source-type MEU-WPT system itself has a 90-degree difference relationship with the voltage. Due to the large equivalent impedance, it can be seen that the impedance angle of the system in the entire frequency band is almost maintained at 72 degrees or above. Under the influence of different voltage configurations and mutual inductance changes, the impedance angles of each excitation unit vary to some extent, but the difference between the resonant currents of the excitation units is relatively small, maintained within 10 degrees. Moreover, when the input voltage of the current source-type MEU-WPT is the same, the influence between the excitation units is very small, but there is still a slight phase bias.

From Figure 5d–f, it can be seen that the input voltage and resonant current phases of a typical voltage source-type MEU-WPT system should be consistent (with an impedance angle of 0). One of the excitation units in the system has a zero-phase angle at the operating frequency point of 80 kHz, but under the influence of input voltage and mutual inductance, the impedance angle even exceeds 180 degrees, and a reverse situation occurs (as shown in Figure 5f in the high-frequency band, negative values occur when the phase exceeds 180), making it impossible for both excitation units to work at a zero-phase angle frequency simultaneously, unless the voltage ratio satisfies a certain mutual inductance relationship equation (as shown in Figure 5d). As shown in the figure, the voltage source-type MEU-WPT cannot use the frequency tracking method of each excitation unit to achieve the maximum power point of the system, because the excitation units do not have a common zero-phase angle frequency. To maximize the output power of the voltage source-type MEU-WPT, the allocation method of the primary power will be discussed in the next section. In contrast, the current MEU-WPT prototype system has better robustness, especially when the input voltage amplitude is consistent, but there are still some phase biases that need to be compensated.

Figure 6 shows the maximum power frequency characteristics of MEU-WPT systems with different input sources observed from the perspective of system operating frequency. Among them, Figure 6a–c shows the current source-type MEU-WPT system, and Figure 6d–f shows the voltage source-type MEU-WPT system.

From Figure 6a–c, it can be seen that the current source-type MEU-WPT system has a unique maximum power operating frequency point of 80 kHz, which is consistent with the design harmonic frequency. However, under the influence of input voltage and mutual inductance changes, there will be some slight frequency drift. For the voltage source-type MEU-WPT system, as shown in Figure 6d–f, there is a significant drift at the frequency point of the maximum power of the entire system when the input voltage and coupling coefficient of the system change. As shown in Figure 6d, when the input voltage is $u_1 = 60$, $u_2 = 30$, and the coupling coefficients $k_1 = 0.15$ and $k_2 = 0.1$, the optimal operating frequency of the system is about 600 kHz. When the coupling coefficients $k_1 = 0.15$ and $k_2 = 0.15$, the optimal power frequency of the system is about 50 kHz, and when the coupling coefficients $k_1 = 0.2$ and $k_2 = 0.15$, the optimal power frequency of the system is about 46 kHz. Similarly, under other input conditions, the optimal power frequency of the system also changes accordingly. For voltage source-type MEU-WPT systems, the maximum power frequency of the system is inconsistent with the operating frequency and the zero-phase frequency of each excitation unit. Although this frequency can achieve maximum power output, impedance changes may bring greater reactive power to the system.

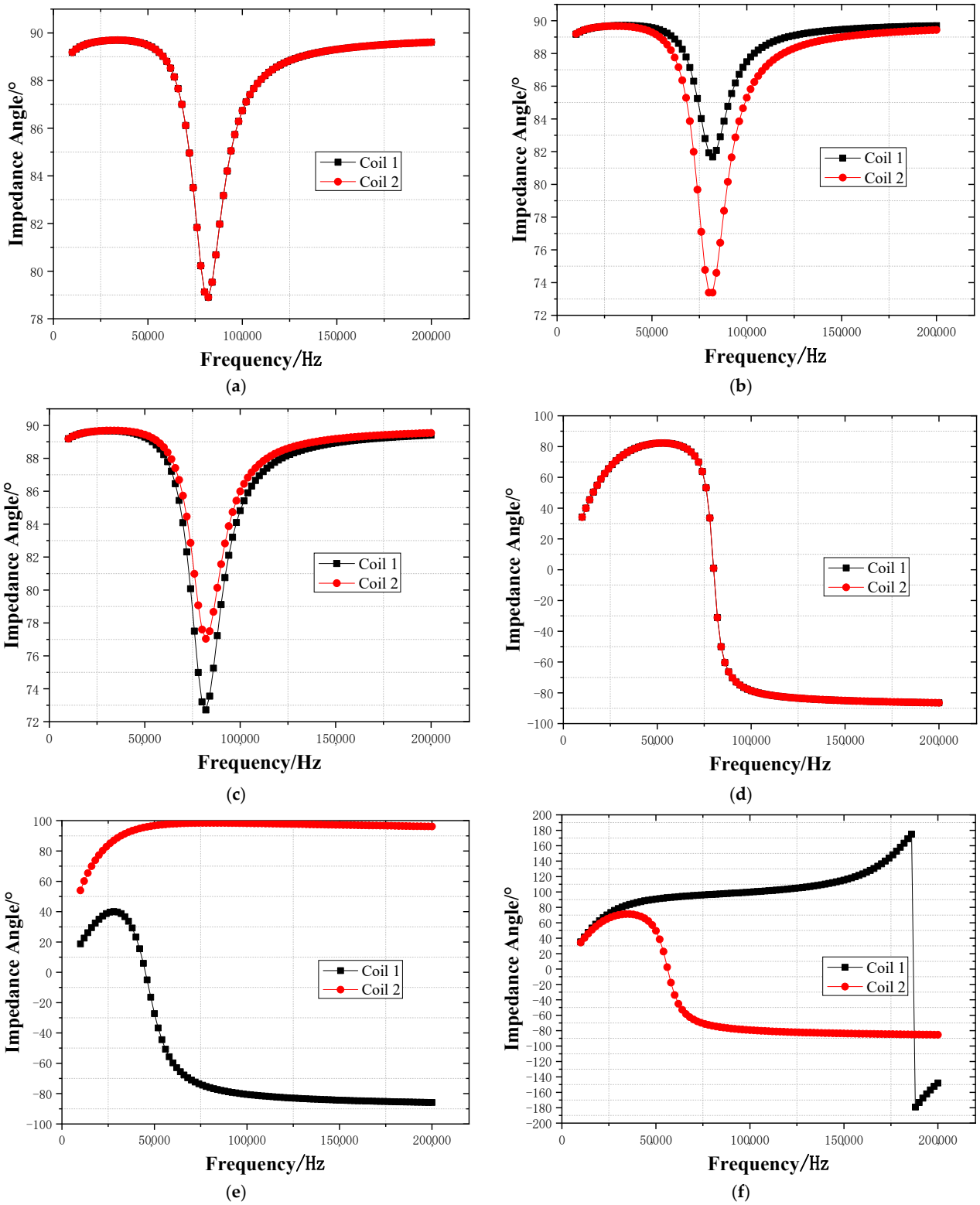

Figure 5. Frequency drifting analysis of single excitation unit. (**a**) The impedance angle results with the current source type when $u_1 = 45$, $u_2 = 45$, $k_1 = 0.15$, $k_2 = 0.15$. (**b**) The impedance angle results with the current source type when $u_1 = 60$, $u_2 = 30$, $k_1 = 0.15$, $k_2 = 0.15$. (**c**) The impedance angle results with the current source type when $u_1 = 45$, $u_2 = 45$, $k_1 = 0.2$, $k_2 = 0.15$. (**d**) The impedance angle results with the voltage source type when $u_1 = 45$, $u_2 = 45$, $k_1 = 0.15$, $k_2 = 0.15$. (**e**) The impedance angle results with the voltage source type when $u_1 = 60$, $u_2 = 30$, $k_1 = 0.15$, $k_2 = 0.15$. (**f**) The impedance angle results with the voltage source type when $u_1 = 45$, $u_2 = 45$, $k_1 = 0.2$, $k_2 = 0.15$.

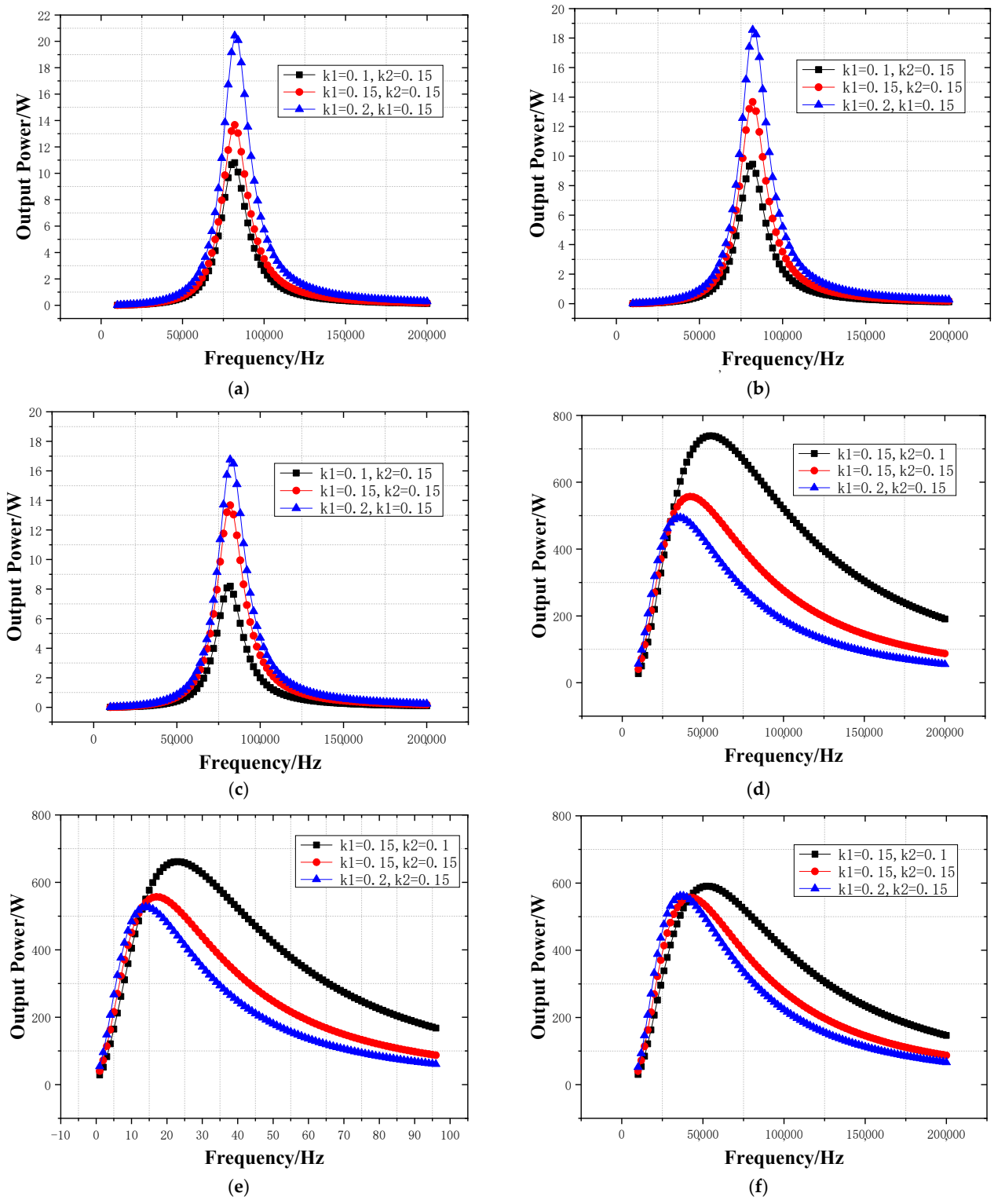

Figure 6. Maximum power frequency analysis of the whole MEU-WPT system. (**a**) The output power results with the current source type when u_1 = 60, u_2 = 30. (**b**) The output power results with the current source type when u_1 = 45, u_2 = 45. (**c**) The output power results with the current source type when u_1 = 30, u_2 = 60. (**d**) The output power results with the voltage source type when u_1 = 60, u_2 = 30. (**e**) The output power results with the voltage source type when u_1 = 45, u_2 = 45. (**f**) The output power results with the voltage source type when u_1 = 30, u_2 = 60.

In summary, when selecting a coil matrix, it is best to choose a current source compensation network or a resonant tank with strong impedance robustness as the topology structure to ensure the frequency stability of multiple coils under working conditions, which means it is better to use LCC or parallel resonance topology or to use a current controller to ensure consistent excitation currents.

5. Experimental Results

The prototype is built. The photo of the MEU-WPT experimental device is shown in Figure 7. Set the system operating frequency f = 100 kHz. The inner diameter of the transmitting coil is 2.15 cm, and the outer diameter is 5.65 cm. The inner diameter of the receiving coil is 5.15 cm, and the outer diameter is 8.4 cm. The DC power supply is 42 V. According to Table 1, the other parameters are given in Table 2.

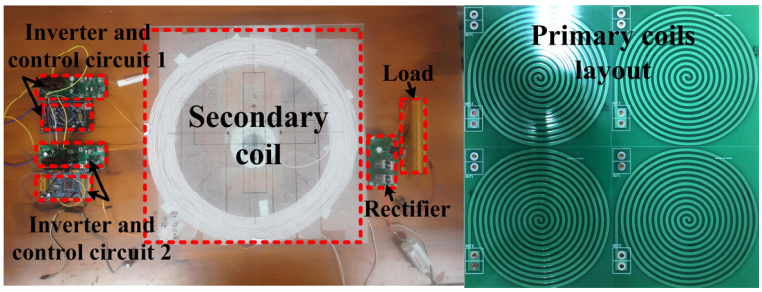

Figure 7. Experimental set-up.

Table 2. Main parameters of the system.

Case	Parameters	Values	Parameters	Values
Four excitation coils-WPT system	$L_{p1}/L_{p2}/L_{p3}/L_{p4}$	20 μH	L_s	120 μH
	R_p	0.05 Ω	R_s	0.12 Ω
	C_{p1}/C_{p2}	0.126 μF	C_s	0.021 μF
	R_L	26 Ω	z	7 cm

When dr = 0 cm, that is, the distance between the four transmitting coils is zero, the output voltage of the system changes as follows with x.

When x = 0 cm, the load voltage is 45.6 V. The waveform before optimization of the drive signal U_1, inverter output voltage $U_{2,}$ and transmitting coil current, as well as the secondary coil current and load voltage, are shown in Figure 8.

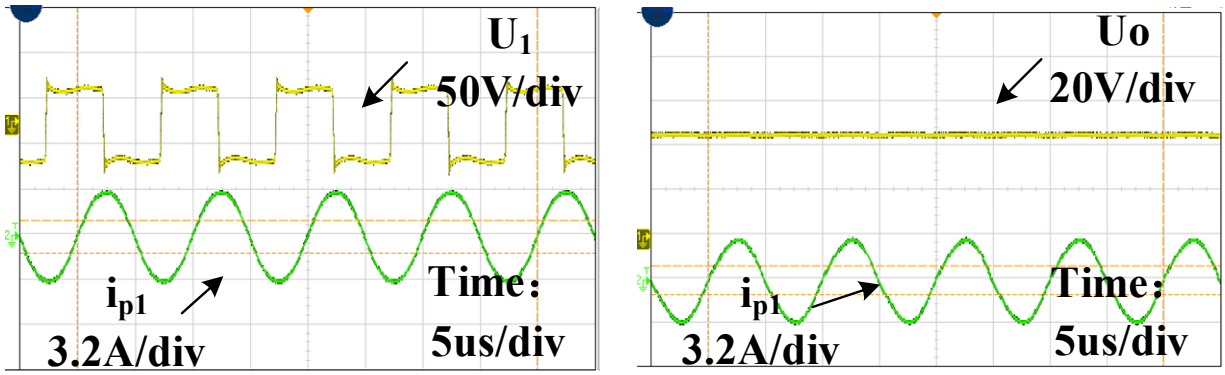

(**a**) (**b**)

Figure 8. Experimental waveform of four-excitation-coil WPT system before optimization: (**a**) waveform of the primary side; (**b**) waveform of the secondary side.

The misalignment testing is shown in Figure 9. When x = 1 cm, the load voltage is 43.3 V, and the secondary coil current and load voltage are shown in Figure 9a. When x = 2 cm, the load voltage is 39.8 V, and the secondary coil current and load voltage are shown in Figure 8b. When x = 3 cm, the load voltage is 35.9 V. The secondary coil current and load voltage are shown in Figure 9c. When x = 4 cm, the load voltage is 30.3 V. The secondary coil current and load voltage are shown in Figure 9d. When x = 5 cm, the load voltage is 28 V. The secondary coil current and load voltage are shown in Figure 9e. When x = 6 cm, the load voltage is 26 V. The secondary coil current and load voltage are shown in Figure 9f. When x = 7 cm, the load voltage is 24.6 V. The secondary coil current and load voltage are shown in Figure 9g.

After the optimal design, when the coil spacing is 1.3 cm, the output voltage of the system varies with X as follows. When x = 0 cm, the load voltage is 41.7 V, and the secondary coil current and load voltage are shown in Figure 10a. When x = 1 cm, the load voltage is 40.6 V. The secondary coil current and load voltage are shown in Figure 10b. When x = 2 cm, the load voltage is 38.6 V. The secondary coil current and load voltage are shown in Figure 10c. When x = 3 cm, the load voltage is 36 V. The secondary coil current and load voltage are shown in Figure 10d. When x = 4 cm, the load voltage is 32.7 V. The secondary coil current and load voltage are shown in Figure 10e. When x = 5 cm, the load voltage is 30.9 V. The secondary coil current and load voltage are shown in Figure 10f. When x = 6 cm, the load voltage is 29.9 V. The secondary coil current and load voltage are shown in Figure 10g. When x = 7 cm, the load voltage is 26.8 V. The secondary coil current and load voltage are shown in Figure 10h. When x = 7.5 cm, the load voltage is 26 V. The secondary coil current and load voltage are shown in Figure 10i.

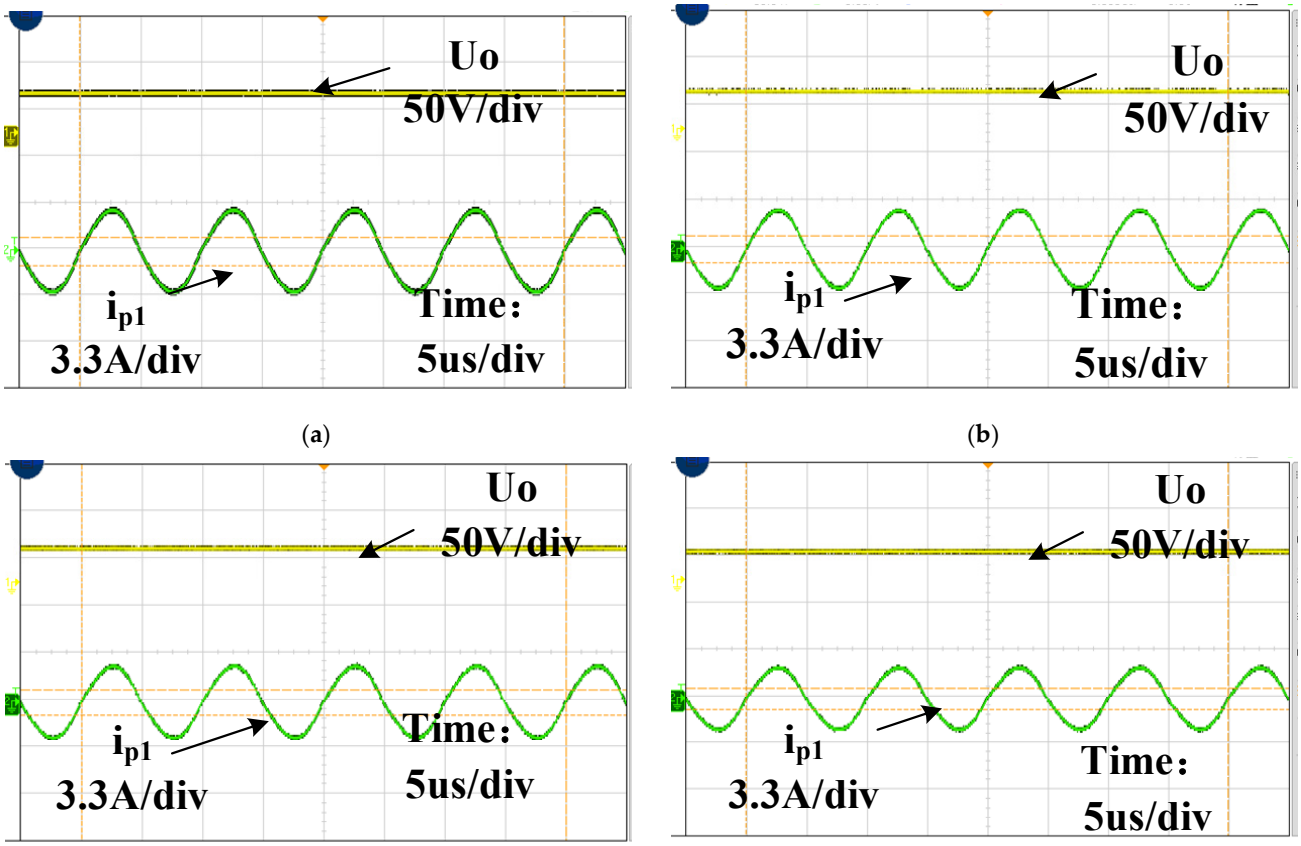

Figure 9. *Cont.*

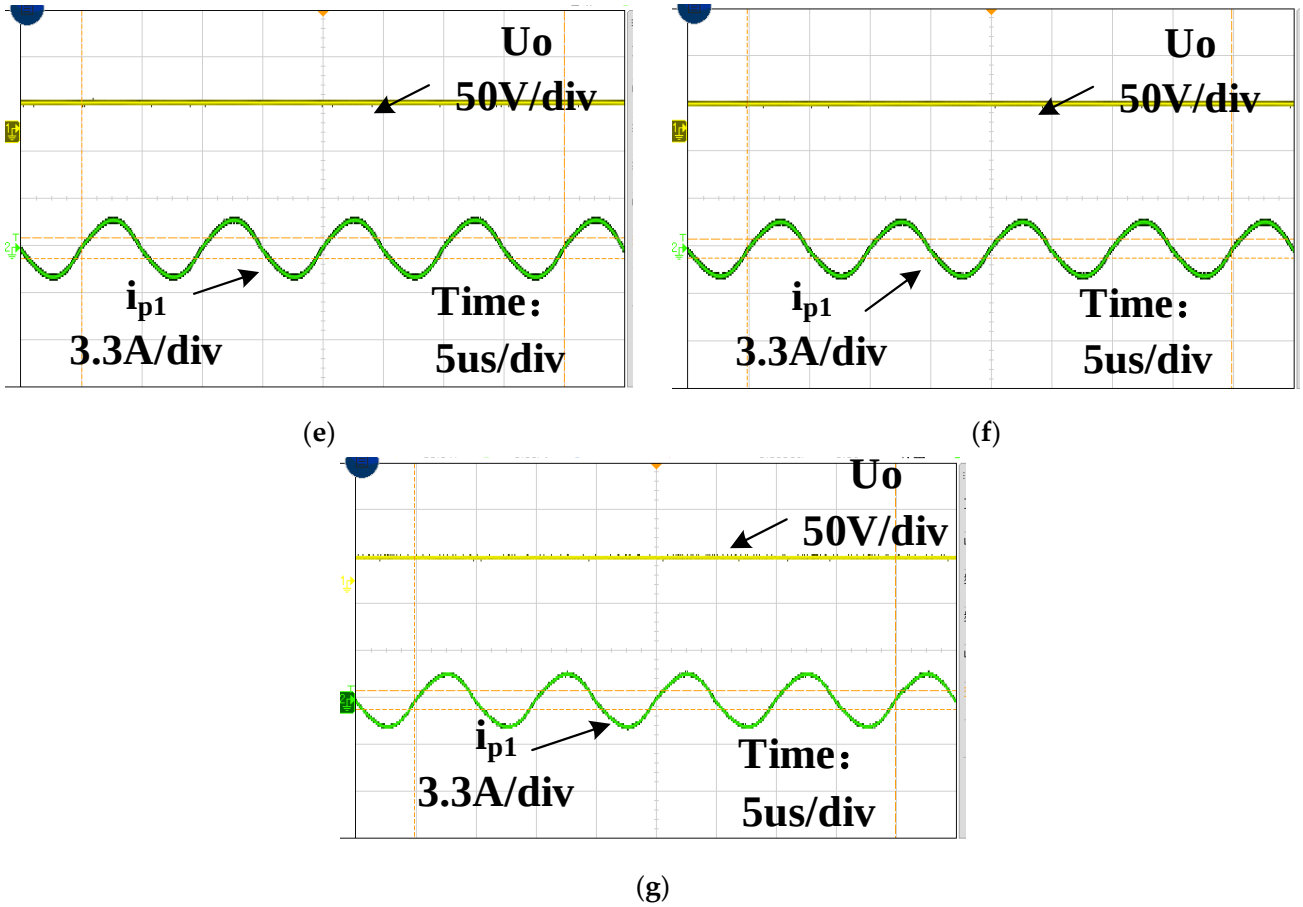

Figure 9. Experimental waveform of misalignment testing before optimal design: (**a**) x = 1 cm; (**b**) x = 2 cm; (**c**) x = 3 cm; (**d**) x = 4 cm; (**e**) x = 5 cm; (**f**) x = 6 cm; (**g**) x = 7 cm.

It can be seen from Figure 11 that when the load resistance is 26 Ω, with the increase in the offset distance, the mutual inductance of the coil will be affected, and the output voltage will finally be affected. When x = 0 cm, the load voltage when the coil spacing is 0 cm is higher than the load voltage when the coil spacing is 1 cm. However, when the output voltage is 26 V, the corresponding receiving coil moving range is from −6 cm to 6 cm. When the coil spacing is 1 cm, the moving range of the receiving coil with the output voltage of 26 V is from −7.5 cm to 7.5 cm, and the offset range is extended by 3 cm. In both cases, there is little fluctuation in the overall efficiency of the system. It can be seen that when the output voltage is stable above 26 V, the offset range of the receiving coil corresponding to the coil spacing of 1 cm is larger, and the misalignment tolerance characteristic of the system is improved to a certain extent.

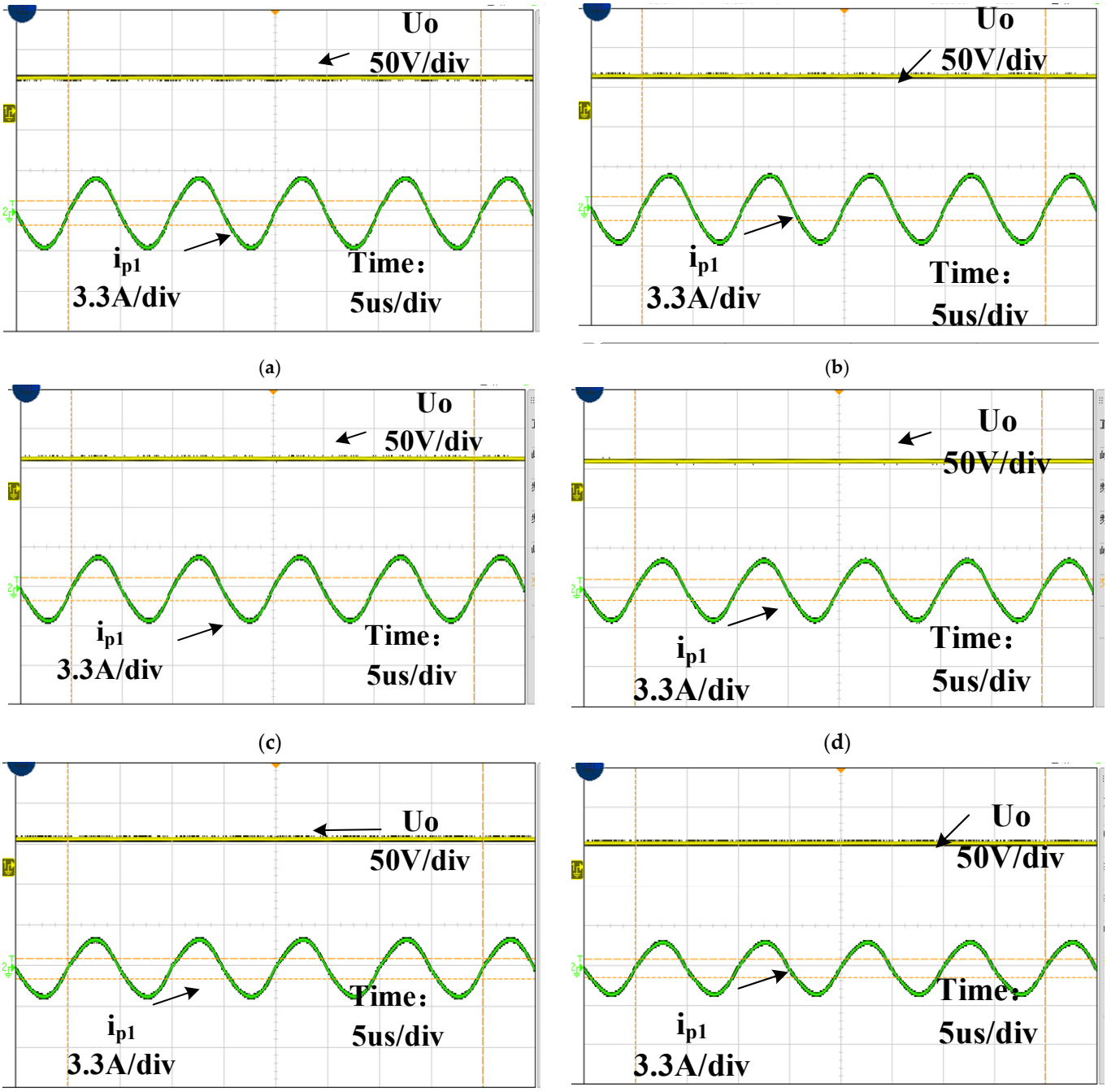

Figure 10. *Cont.*

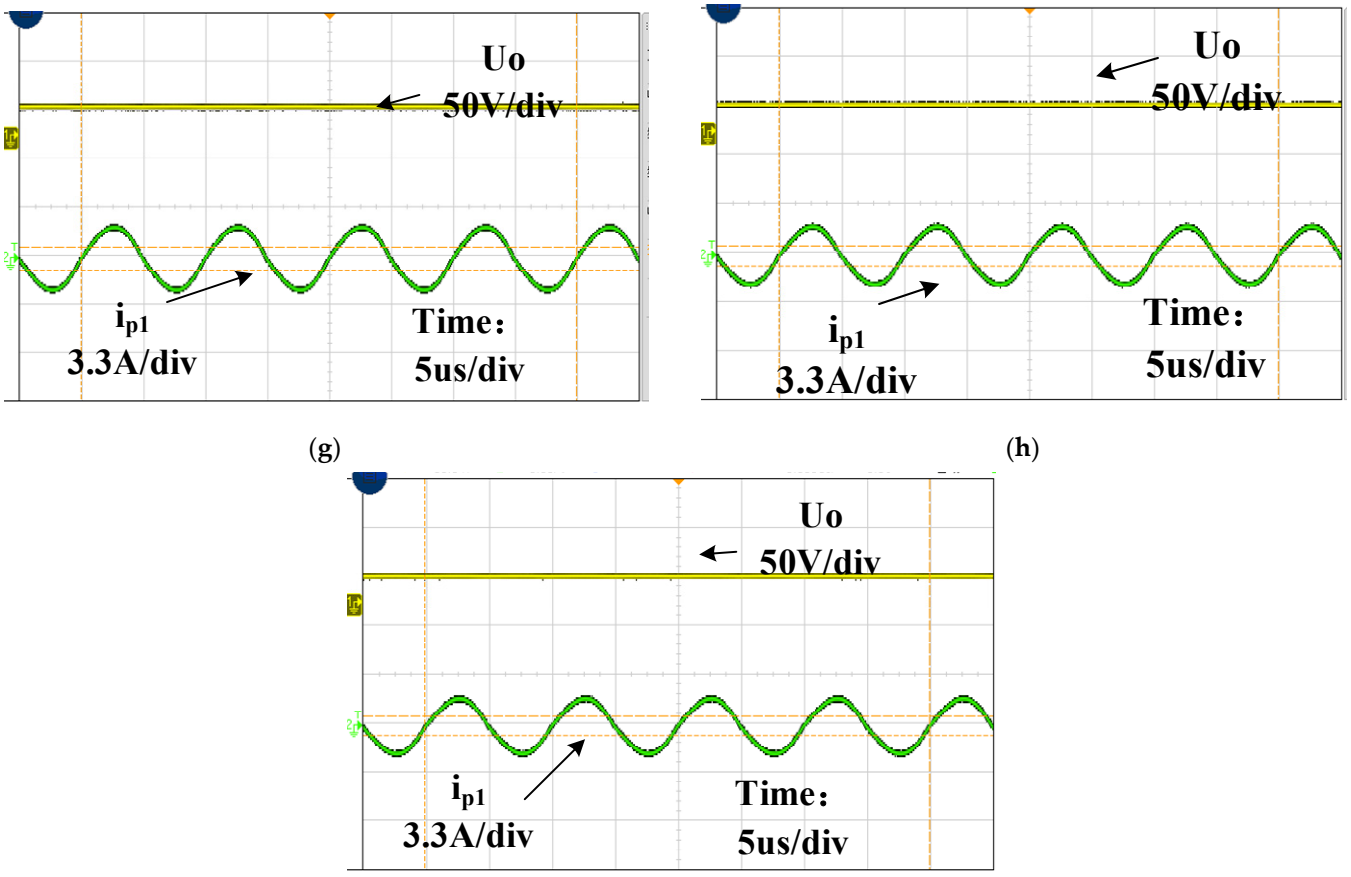

Figure 10. Experimental waveform of misalignment testing after optimal design: (**a**) x = 0 cm; (**b**) x = 1 cm; (**c**) x = 2 cm; (**d**) x = 3 cm; (**e**) x = 4 cm; (**f**) x = 5 cm; (**g**) x = 6 cm; (**h**) x = 7 cm; (**i**) x = 7.5 cm.

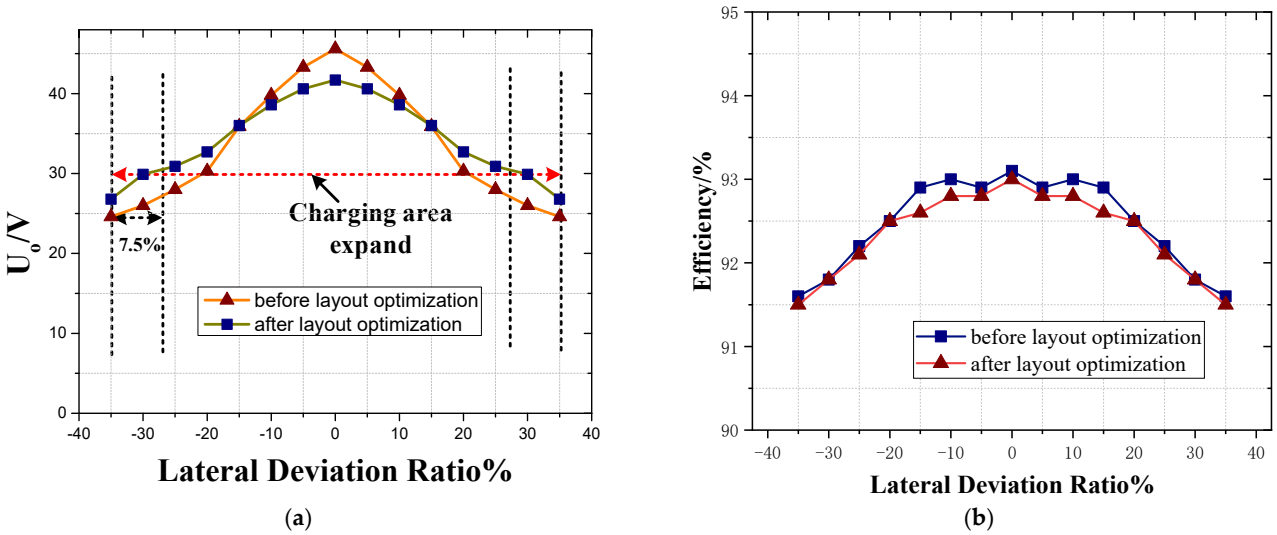

Figure 11. Charging area comparison: (**a**) comparison of output voltage; (**b**) comparison of efficiency.

The comparison is shown in Figure 11.

6. Conclusions

This paper analyzes the charging area division and optimization of the MEU-WPT system using matrix coils. Firstly, the circuit architecture of the MEU-WPT system is analyzed. Moreover, based on electromagnetic theory and the Neumann equation, the mutual inductance changes in the system under a given coupling mechanism are studied. On the basis of establishing a spatial coordinate system, combined with the output characteristic formula derived from the circuit model, the distribution of output power in space is described. At the same time, indicators are provided for the charging area of the system, and they are used to divide the effective charging area of the MEU-WPT system, which can help to calculate the charging area. Then, the projection area of the charging area is extended as the optimization objective, and the expression and constraint conditions for the charging area are obtained. Furthermore, in order to reduce the interference of adjacent coils in the working mode of the matrix coupling mechanism, a comparative analysis was conducted on the frequency stability of each unit with different resonant topologies, and recommendations for circuit selection are provided. Finally, experimental verification was conducted using the analysis method of the previous charging area, and the design method proposed in this paper improved the effective charging area by 15% compared to traditional design methods.

Author Contributions: Conceptualization, J.J. and Z.M.; methodology, J.J.; software, J.J.; validation, Z.M.; formal analysis, J.J.; investigation, J.J.; resources, J.J.; data curation, Z.M.; writing—original draft preparation, J.J.; writing—review and editing, J.J.; visualization, Z.M.; supervision, Z.M.; project administration, J.J.; funding acquisition, J.J. All authors have read and agreed to the published version of the manuscript.

Funding: The research is supported by the National Key R&D Program of China under grant 2022YFF0604200 and the Natural Science Foundation Postdoctoral Science Foundation Project of Chongqing under grant cstc2021jcyj-bshX0245 and cstc2021jcyj-bshX0159.

Data Availability Statement: Data are contained within the article.

Conflicts of Interest: The authors declare no conflict of interest.

References

1. Luo, Z.C.; Zhao, Y.Y.; Xiong, M.; Wei, X.Z.; Dai, H.F. A Self-Tuning LCC/LCC System Based on Switch-Controlled Capacitors for Constant-Power Wireless Electric Vehicle Charging. *IEEE Trans. Ind. Electron.* **2022**, *70*, 709–720. [CrossRef]
2. Zhang, Z.; Pang, H.; Georgiadis, A.; Cecati, C. Wireless power transfer—An overview. *IEEE Trans. Ind. Electron.* **2018**, *66*, 1044–1058. [CrossRef]
3. Zhang, Y.; Chen, S.; Li, X.; Tang, Y. Design of high-power static wireless power transfer via magnetic induction: An overview. *CPSS Trans. Power Electron. Appl.* **2023**, *6*, 281–297. [CrossRef]
4. Van Mulders, J.; Delabie, D.; Lecluyse, C.; Buyle, C.; Callebaut, G.; Van der Perre, L.; De Strycker, L. Wireless Power Transfer: Systems, Circuits, Standards, and Use Cases. *Sensors* **2022**, *22*, 5573. [CrossRef] [PubMed]
5. Ahmed, K.T.; Ali, Y.; Heath, R.W. Optimization of Power Transfer Efficiency and Energy Efficiency for Wireless-Powered Systems with Massive MIMO. *IEEE Trans. Wirel. Commun.* **2018**, *17*, 7159–7172.
6. Liu, J.; Liu, Z.; Chen, W.; Sun, Z.; Su, H. An Optimized Coil Array and Passivity-Based Control for Receiving Side Multilevel Connected DC-DC Converter of Dynamic Wireless Charging. *IEEE Trans. Veh. Technol.* **2022**, *71*, 3715–3726. [CrossRef]
7. Dai, X.; Jiang, J.C.; Wu, J.Q. Charging Area Determining and Power Enhancement Method for Multi-Excitation Unit Configuration of Wirelessly Dynamic Charging EV System. *IEEE Trans. Ind. Electron.* **2018**, *5*, 4086–4096.
8. Hou, X.; Hu, H.; Su, Y.; Liu, Z.; Deng, Z.; Deng, R. A Multirelay Wireless Power Transfer System with Double-Sided LCC Compensation Network for Online Monitoring Equipment. *IEEE J. Emerg. Sel. Top. Power Electron.* **2022**, *11*, 1262–1271. [CrossRef]
9. Li, J.; Wang, C.; Wang, L.; Ding, Y.; Yu, T.; Cheng, Y. A Comparative Study on Transmission Performance of Multistage Wireless Power Transfer Systems Using SPS Compensation and LCC Compensation. *Int. J. Circuit Theory Appl.* **2022**, *51*, 1625–1641. [CrossRef]
10. Li, H.; Wang, K.; Huang, L.; Chen, W.J.; Yang, X. Dynamic Modeling Based on Coupled Modes for Wireless Power Transfer Systems. *IEEE Trans. Power Electron.* **2015**, *30*, 6245–6253. [CrossRef]
11. Cao, Y.; Qahouq, J.A.A. Analysis and evaluation of input power splitting method between multiple transmitters for maximum wireless power transfer. In Proceedings of the 2018 IEEE Applied Power Electronics Conference and Exposition (APEC), San Antonio, TX, USA, 4–8 March 2018; pp. 959–962.

12. Zargham, M.; Gulak, P.G. Maximum Achievable Efficiency in Near-Field Coupled Power-Transfer Systems. *IEEE Trans. Biomed. Circuits Syst.* **2012**, *6*, 228–245. [CrossRef] [PubMed]
13. Kim, S.; Kwon, N.; Ahn, S.; Lee, W. Three-Dimensional Wireless Power Transfer System Using Multiple Orthogonal Resonators for Spatial Freedom. *IEEE Trans. Antennas Propag.* **2023**, *71*, 4036–4044. [CrossRef]
14. Li, X.; Wang, C.; Wang, H.; Dai, X.; Sun, Y.; Hu, A.P. A Robust Wireless Power Transfer System with Self-Alignment Capability and Controllable Output Current for Automatic-Guided Vehicles. *IEEE Trans. Power Electron.* **2023**, *38*, 11898–11906. [CrossRef]
15. Li, S.; Li, W.; Deng, J.; Nguyen, T.D.; Mi, C. A Double-Sided LCC Compensation Network and Its Tuning Method for Wireless Power Transfer. *IEEE Trans. Veh. Technol.* **2015**, *64*, 2261–2273. [CrossRef]
16. Zhou, S.; Mi, C. Multi-Paralleled LCC Reactive Power Compensation Networks and Their Tuning Method for Electric Vehicle Dynamic Wireless Charging. *IEEE Trans. Ind. Electron.* **2016**, *63*, 6546–6556. [CrossRef]
17. Xu, C.; Zhuang, Y.; Han, H.; Song, C.; Huang, Y.; Zhou, J. Multi-coil high efficiency wireless power transfer system against misalignment. In Proceedings of the 2018 IEEE MTT-S International Wireless Symposium (IWS), Chengdu, China, 6–10 May 2018; pp. 1–3.
18. Qiao, T.; Yang, X.; Lai, X.; Tang, H. Modeling and Analysis of Multi-Coil Magnetic Resonance Wireless Power Transfer Systems. In Proceedings of the 2018 IEEE PELS Workshop on Emerging Technologies: Wireless Power Transfer (Wow), Montreal, QC, Canada, 3–7 June 2018; pp. 1–6.
19. Liu, Y.; Kamineni, A.; Ukegawa, H.; Dede, E.M.; Lee, J.S. Multi-layer Design and Power Transfer Test of PCB-Based Coil for Electric Vehicle Wireless Charging. In Proceedings of the 2023 IEEE Wireless Power Technology Conference and Expo (WPTCE), San Diego, CA, USA, 4–8 June 2023; pp. 1–5.
20. Kim, J.; Kang, W.; Ku, H. A Study on Wireless Power Transfer of Small Device using Multi-Layer Coil. In Proceedings of the 2018 International Symposium on Antennas and Propagation (ISAP), Busan, Republic of Korea, 23–26 October 2018; pp. 1–2.
21. Liao, S.; Xu, Z.; Zhu, J.; Chen, Z. Multi-Transmitter Coils Optimization for Range-Adaptive Wireless Power Transfer by Using Genetic Algorithm. In Proceedings of the 2023 IEEE MTT-S International Wireless Symposium (IWS), Qingdao, China, 14–17 May 2023; pp. 1–3.
22. Raju, S.; Wu, R.; Chan, M.; Yue, C.P. Modeling of Mutual Coupling Between Planar Inductors in Wireless Power Applications. *IEEE Trans. Power Electron.* **2013**, *29*, 481–490. [CrossRef]
23. Grover, F.W. *Inductance Calculation: Working Formulas and Tables*; Dover: New York, NY, USA, 1946.
24. Tan, L.; Huang, X.L.; Zhao, J.F.; Zhao, J.M.; Wang, W.; Zhou, Y. Optimization Design for Disc Resonators of a Wireless Power Transmission System. *Trans. China Electrotech. Soc.* **2013**, *28*, 1–6.
25. Wojda, R.P.; Kazimierczuk, M.K. Winding resistance of litz-wire and multi-strand inductors. *IET Power Electron.* **2012**, *5*, 257–268. [CrossRef]

Disclaimer/Publisher's Note: The statements, opinions and data contained in all publications are solely those of the individual author(s) and contributor(s) and not of MDPI and/or the editor(s). MDPI and/or the editor(s) disclaim responsibility for any injury to people or property resulting from any ideas, methods, instructions or products referred to in the content.